Effects of Porosity in Graphite Materials on Ablation in Arc-Heated Jets

Irving Auerbach,* Morton L. Lieberman,* Katheryn E. Lawson,† and Hugh O. Pierson*
Sandia Laboratories, Albuquerque, N. Mex.

The ablation performance of chemically vapor-deposited carbon on a carbon felt made from polyacrylonitrile fiber, ATJ-S, and ATJ-S percursor graphites was studied in an arc jet at stagnation pressures and bulk gas enthalpies of 2.2 to 10.3 MPa and 4700 to 5800 J/g, respectively. The initial nonlinear ablation kinetics is associated with the attainment of thermal and chemical equilibrium. In the subsequent steady-state period, the ablation rate is constant. Ablation was modeled with an exponential rate relationship and the steady-state rate constants were shown to be related exponentially to porosity. A scanning electron microscope examination of ablated surfaces showed that nonuniform surface ablation can be correlated with porosity, fiber density, and the fiber-matrix interfacial spacing.

Introduction

THE ablation of a thermal protective material on a re-entry vehicle, e.g., graphite, phenolic composites, etc., is a surface phenomenon and is, therefore, subject to the porosity of the protective material. This study addresses the effect of porosity on ablation performance for two types of graphitic materials: 1) ATJ-S and its precursors, and 2) a carbon/carbon composite prepared by chemically vapor-depositing carbon on a polyacrylonitrile precursor felt (CVD/PAN). Although carbon/carbon composites prepared from rayon precursor felts (CVD/rayon) have been used for aft heat shields on re-entry vehicles, the improved thermal stress resistance of the CVD/PAN composite suggested that it could be used for nose tips.

It was anticipated that porosity would be an important factor in the ablation performance of the CVD/PAN composite. For this reason, ATJ-S graphite and ATJ-S precursors, one of which had received no impregnation and the other of which had received one impregnation, were included in the test matrix for comparison. This paper provides the results of this study. A more detailed report is given in Ref. 1.

Experimental

Test Facilities

The Sandia 2 MW[2] and the McDonnell Douglas HIP[3] arc heaters were used to study the ablation performance of the materials included in this paper. The Sandia facility consists of a Linde N-1000 arc heater which exhausts through a supersonic nozzle (Mach 1.7 and throat diameter of 0.70 cm) and a 1.02 cm exit into a test chamber maintained at pressures below 6500 Pa. The McDonnell Douglas HIP facility uses the MDC-200 arc heater which has a Mach 1.7 nozzle, a 0.953-cm diam throat, and an exit diameter of 1.14 cm which exhausts into an ambient environment. In both systems, models were injected into the heat exhaust by a Ferguson Intermitter at a fixed position of 0.25 cm from the nozzle exit. A maximum of five models was tested in a single test run. Two injector arms held a pitot probe and a null point calorimeter for pressure and heat-flux measurements. Bulk enthalpies were obtained from energy balance measurements on the arc heater. The stagnation pressures used in the Sandia and HIP facilities were 2.3 to 2.5 and 10.3 MPa, respectively. The bulk gas enthalpies were nominally 5200 to 5800 and 4700 J/g, respectively.

Materials

Five types of graphitic materials were studied: CVD/PAN, commercial ATJ-S, and three graphites specially prepared by Union Carbide, namely, nonimpregnated and singly impregnated ATJ-S precursors and fully impregnated ATJ-S obtained from these precursors. The CVD/PAN carbon/carbon composites were fabricated by carbonization of the PAN felt, infiltration of the carbon matrix by pyrolysis of methane, and graphitization of the material at 3000°C. The models used in the Sandia test facility were obtained from two frusta designated 4A and 6A. Details of the fabrication conditions employed in their preparation are given in Ref. 4. The material tested in the HIP facility was obtained from plates prepared under similar conditions.

The nonimpregnated, singly impregnated, and fully impregnated ATJ-S, which had been obtained from a single precursor billet and which had been graphitized under the same conditions, provided the opportunity to study the effect of porosity on ablation with materials possessing minimal differences. Sections were cut during each step of the process and graphitized. Commercial ATJ-S models were included in each run as controls, along with CVD/PAN and the specially processed ATJ-S and its precursors.

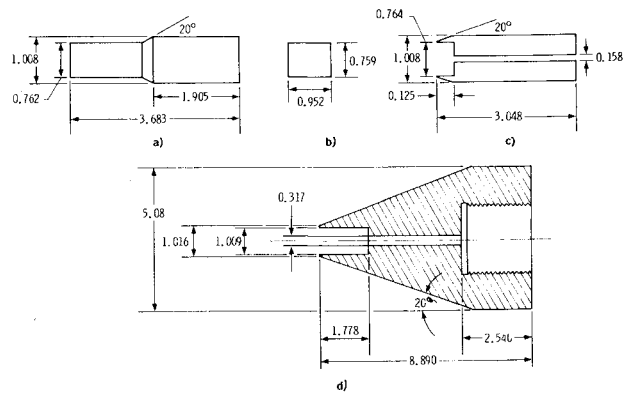

Fig. 1 Models and model holders. All dimensions in centimeters. a) Model used for CVD/PAN 6A series, ATJ-S, and ATJ-S graphite precursors. b) Model used for CVD/PAN 4A series and ATJ-S graphite. c) Model holder for model in Fig. 1b which interfaces with holder in Fig. 1d. d) Phenolic-Refrasil model holder which interfaces with arc-heater assembly.

Received Aug. 27, 1976.
Index categories: Material Ablation, Thermochemistry and Chemical Kinetics.

*Member of the Technical Staff.

†Member of the Technical Staff; present address: Bendix Corporation Research Laboratories, Southfield, Mich.

Test Models

Two test-model designs were used. The design in Fig. 1a was used for material from frustum 6A and the plates. To attain the dimensions in this figure, the models were cut in the longitudinal direction of the frustum. To study the ablation performance of surfaces normal to the radial direction, shorter sections with dimensions in Fig. 1b were cut from the center of the inner and outer surfaces of frustum 4A where the densities were more uniform. These models were interfaced with the Ferguson Intermitter injection system through the ATJ-S graphite and phenolic-Refrasil holders (Figs. 1c and 1d). The models were selected from several sections of the frustum to obtain a range of porosities.

Data Acquisition

Model recession was photographed at 200 frames/sec on microfilm and a Boscar Film Reader was used to measure recession as a function of frame number and time.

Porosity Measurements

Pore volumes of the materials were measured by quantitative television microscopy. The Quantimet 720 image analyzing computer (trade name of IMANCO, Ltd., Melbourne, England), which differentiates the pores from the matrix material by differences in optical reflectivities, was used for the measurements. A detailed description of the instrument is given in Ref. 5. Briefly, an image from a specimen or a photograph is focused onto a television camera which converts the optical image into an electronic image for detection. Features of interest are distinguishable from unwanted features on the basis of gray-level criteria. The output of the detector then is fed into a computer module for computation of the desired parameter.

Two techniques were used with this instrumentation. For the full-sized graphite models (Fig. 1a), the top surfaces were projected with a Leitz Orthoplan microscope operated at 124×. For the small-sized models (Fig. 1b), 10× photographs were made and examined using an epidiascope fitted with a 7× lens as image source, giving a second magnification of 70×. Typically, the pores, as shown in Fig. 2, appear as dark features and in sufficient contrast against the lighter graphite matrix to isolate the pore boundaries. For an assumed spherical geometry of the pores, the lower limits of detection for the two image sources (microscope and epidiascope) are 2 and 4 μm, respectively.

Direct microscopic observation is preferred because a broader range of magnification is available. With the epidiascope, photographic magnification becomes the limiting factor and this, in turn, is limited by the model and print size. When the CVD/PAN 4A models were studied, however, the epidiascope was the only operational mode available on the Quantimet at that time.

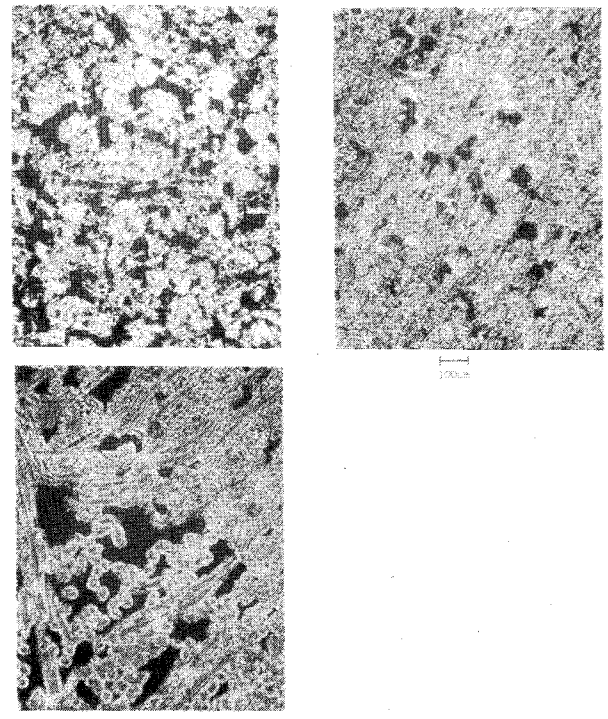

Fig. 2 Representative graphite surfaces showing porosity variation. Upper left: ATJ-S precursor, not impregnated; upper right: ATJ-S graphite; lower left: CVD/PAN 6A.

For the CVD/PAN 6A models, both the epidiascope and microscope were used to measure the porosities. Data from both techniques provided a method for comparing the relative porosities of models with pore sizes greater than 2 and 4 μm. In addition to using both techniques for pretest or virgin-material measurements in the 6A models, post-test porosities were measured microscopically about 5 mm below the ablated surface so that a scaling factor could be obtained to convert the porosities of the 4A series of models to comparable porosities for the 6A series and thereby permit a composite plot of all of the models studied. The lack of definition in the 10× photographs made this conversion questionable.

Results and Discussion

Porosity

Percent porosity should be related to density through the following relationship:

$$\text{porosity} = [1 - (\text{density}/2.26)] \times 100 \qquad (1)$$

Table 1 Comparative measured and computed porosities

Material	Number of models	Measured density: Before testing, g/cm^3	$\hat{s}$[a]	Measured density: After testing, g/cm^3	$\hat{s}$	Measured porosity: Before testing, %	$\hat{s}$	Measured porosity: After testing, %	$\hat{s}$	Computed porosity: Before testing, %	Computed porosity: After testing, %
CVD/PAN 6A series	6	1.818	0.0098	1.811	0.0170	16.8	2.32	31.8	5.31	19.6	19.9
ATJ-S precursors											
No impregnations	3	...	...	1.519	0.0143	...	...	29.8	3.83	...	32.8
One impregnation	5	...	...	1.752	0.0047	...	...	21.1	2.43	...	22.5
ATJ-S from above precursors (Two impregnations)	1	...	...	1.830	...	...	...	20.6	...	...	19.0
Commercial ATJ-S	5	...	...	1.845	0.0117	...	...	19.4	3.78	...	18.3

[a] $\hat{s}$ = Standard deviation.

where 2.26 is the density of nonporous single crystal graphite. Table 1 compares the computed and measured porosities for most of the materials studied. The correlation is good, with the exception of the CVD/PAN 6A graphites. In this case, the computed porosity, 19.6 to 19.9%, is comparable with the measured pretest porosity of 16.8% but not with the post-test value of 31.8%. Obviously, the material just below the ablated surface (about 5 mm) has become more porous than that in the bulk. This phenomenon was observed only in the 6A material. The post-test porosities of the ATJ-S and precursor graphites below the ablated surfaces compared favorably with their calculated porosities (Table 1). Porosities of pretest or virgin material were, therefore, not measured.

Ablation

The ablation results of the CVD/PAN 6A, ATJ-S, and ATJ-S precursor models obtained with the larger test model design (Fig. 1a) provided a broader spectrum of material types and porosities and more precise data. Typical recession vs time curves are shown in Fig. 3. These curves always show an initial nonlinear kinetics phase, during which thermal and chemical equilibrium conditions are approached, and a subsequent linear or steady-state phase, in which the recession rate appears to be constant. Deviations from linearity after the steady-state condition was attained were observed where recession exceeded 0.5 cm. This was due to the model leaving the constant environment zone in the arc jet. The steady-state condition generally provides a convenient source for evaluating a rate constant in comparative studies. However, the high-porosity materials tended to develop grossly roughened surfaces (visual to the eye) during the latter portion of the initial phase. Thus, a comparison of rate constants in the steady-state phase is a comparison of models with different gross surface areas. It was, therefore, desirable to obtain an estimate of the initial ablation rates when the gross surface areas were equivalent, as well as the steady-state rates, to see how the intrinsic porosity affected the ablation rate of a smooth surface. To evaluate rate constants that governed the initial nonsteady-state phase before roughness developed, an exponential relationship, given below, was assumed. Although the relationship is empirical, its conformity with experimental results justifies comparisons of its parameters with material properties and the computation of extrapolated ablation rates

$$s = k_1 (1 - e^{-k_2 t}) t \tag{2}$$

where s = recession, cm; k_1 = steady-state rate constant, cm/sec; k_2 = nonsteady-state rate constant, $\sec^{-1}$; and t = time, sec.

Equation (2) is approximate because k_1 is expressed as a function of k_2 and time rather than model temperature, which is primarily responsible for the ablation rate and mechanism. Temperature, in turn, is dependent on the heat flux and the material properties. Because temperature and heat flux data were not always available, k_2 was used as an alternate parameter for correlations involving material type and porosity.

The rate constants were evaluated in the following manner. Values for k_1 were obtained from s/t values at extended times when $e^{-k_2 t}$ approached zero and s/t became constant. Values for k_2 then were obtained from the following rearranged form of Eq. (2)

$$\ln [k_1 - (s/t)] = -k_2 t + \ln k_1 \tag{3}$$

Plots of $\ln [k_1 - (s/t)]$ vs t were linear and their slopes provided values for k_2.

The adequacy of Eq. (2) for modeling ablation under the conditions of this study is shown in sample plots in Fig. 4. A log-log format is used to emphasize the correlation over the entire range of time and recession covered.

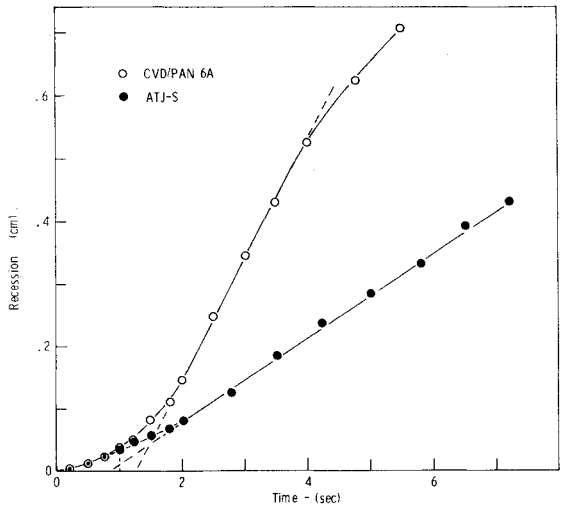

Fig. 3 Representative recession vs time plot for ATJ-S and CVD/PAN 6A showing initial and steady-state phases.

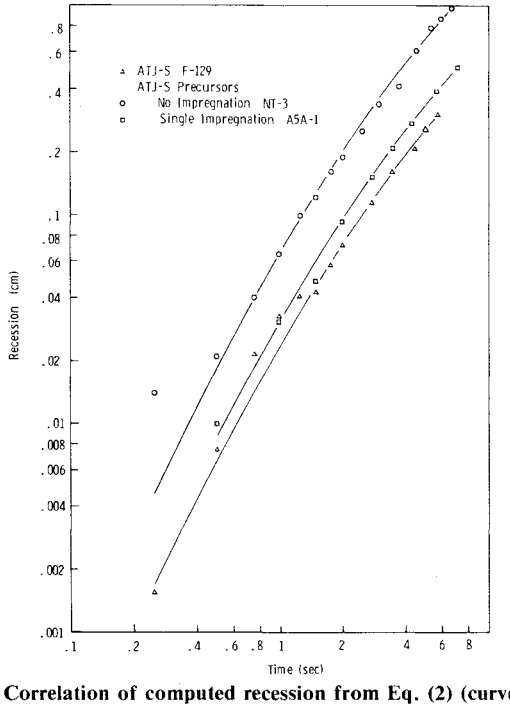

Fig. 4 Correlation of computed recession from Eq. (2) (curve) and experimental values (symbols).

Stagnation pressure and bulk enthalpy varied from test to test over a small but significant range. It was, therefore, necessary to normalize k_1 and k_2 for these variations before they were used for correlations with porosity. The normalization relationship is given below

$$k = A_s(k) \cdot P_{t_2} \cdot H_0^2 / r^{1/2} \tag{4}$$

where

$A_s(k)$ = normalized recession rate constant;
for k_1, the units are $(\text{cm}^{3/2}\,\text{g}^2)/(\text{sec Pa J}^2)$
for k_2, the units are $(\text{cm}^{1/2}\,\text{g}^2)/\text{sec Pa J}^2)$
P_{t_2} = stagnation pressure, Pa
H_0 = bulk gas enthalpy, J/g
r = model radius, cm

In addition to the recession rate constant $A_s(k_1)$, a mass-transfer rate constant was calculated from the following relationship

$$A_m(k_1) = A_s(k_1) \cdot \rho \tag{5}$$

where

$A_m(k_1)$ = mass-transfer rate constant, $g^3/cm^{3/2}sec\ Pa\ J^2$
ρ = density, g/cm^3

A similar conversion for k_2 is not justified since k_2 has the dimensions of sec^{-1}.

Mean values for the porosities, $A_s(k_1)$, $A_s(k_2)$, and $A_m(k_1)$ are given in Table 2. A regression analysis of porosity vs $A_s(k_1)$ data, in which polynominals and a log relationship were considered, showed that the best correlation was obtained with the log relationship. The value for the correlation coefficient

$$\left(\frac{\sum (x-\bar{x})(y-\bar{y})}{\sqrt{\sum (x-\bar{x})^2 \sum (y-\bar{y})^2}} \right)^2$$

for the log vs porosity plot was 0.990. The correlation is surprisingly good in view of the large standard deviations for values of k_1 and porosities.

Figure 5 shows a plot of the data and the curve described by the following equation

$$A_s(k_1) = 0.871\ e^{0.0782P} \qquad (6)$$

where P is porosity in percent. The exponential relationship between $A_s(k_1)$ and P emphasizes the deleterious effect of porosity on the ablation rate, especially at the higher porosities but also in the lower range. Thus, the ablation rate of ATJ-S presumably could be reduced by one-half if the porosity were reduced to 10% or its density increased to 2.03 g/cm^3.

A similar plot is obtained for the normalized mass-transfer rate constant $A_m(k_1)$ vs porosity (Fig. 6). Two values are plotted for CVD/PAN 6A, one obtained from the bulk density and the other from the density below the ablation surface, 1.541 g/cm^3. The latter value was computed from Eq. (1) using the post-test porosity value of 31.8%. For the other materials, the bulk densities were used, since the porosities below the ablation surface were similar to those for the bulk material.

The existence of a lower than bulk density material below the ablation surface of the CVD/PAN 6A models is supported by Fig. 5, since the $A_m(k_1)$ value obtained from the density below the ablation surface conforms with the plot. This result emphasizes the importance of the in-depth decrease in density during ablation and the resultant higher local porosity. It also suggests that CVD/PAN 6A would ablate at about the same rate as ATJ-S if the porosity did not change during ablation. The increase in porosity below the surface may have been due to material removal caused by oxidation, although this mechanism has not been established.

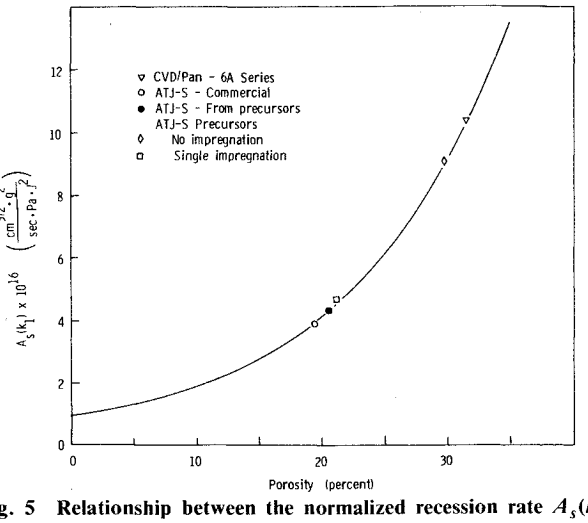

Fig. 5 Relationship between the normalized recession rate $A_s(k_1)$ and porosity. Curve was obtained by regression analysis of the data assuming the relationship in Eq. (6).

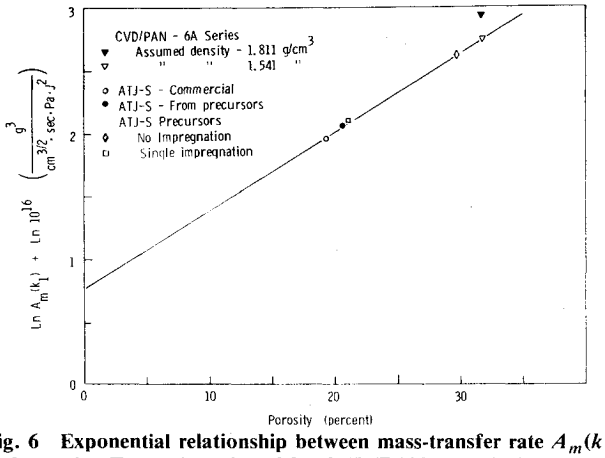

Fig. 6 Exponential relationship between mass-transfer rate $A_m(k_1)$ and porosity. Two points plotted for CVD/PAN show the importance of the lower density value in computing mass transfer for this material.

Correlations between $\ln A_s(k_1)$ and porosity measured by the preceding correlation coefficient within any one material group were poor to nonexistent. An exception was the nonimpregnated ATJ-S. This apparent contradiction, where a correlation exists between the mean values of the groups and not within a group, may be because the range of values for

Table 2 Mean values for porosities and rate constants

	Number of models	Mean post-test porosity, %	$\hat{s}$[a]	Mean $A_s(k_1)$, $\left(\frac{cm^{3/2}g^2}{sec\text{-}Pa\text{-}J^2}\right)$	$\hat{s}$	Mean $A_s(k_2)$, $\left(\frac{cm^{1/2}g^2}{sec\text{-}Pa\text{-}J^2}\right)$	$\hat{s}$	Mean $A_m(k_1)$, $\left(\frac{g^3}{cm^{3/2}\text{-}sec\text{-}Pa\text{-}J^2}\right)$
CVD/PAN								
6A series	6	31.8	5.31	10.34×10^{-16}	2.04×10^{-16}	4.46×10^{-15}	0.99×10^{-15}	$18.73^b \times 10^{-16}$
								15.93^c
ATJ-S precursors								
No impregnations	3	29.8	1.79	9.06	1.66	4.48	0.56	13.76
One impregnation	5	21.1	2.43	4.68	1.92	4.55	0.64	8.20
ATJ-S from above precursors (Two impregnations)	1	20.6	...	4.34	...	4.44	...	7.94
Commercial ATJ-S	5	19.4	3.78	3.88	0.29	3.88	0.88	7.16

[a] s = Standard deviation. [b] $A_m(k_1)$ value based on density value of 1.811 g/cm^3. [c] $A_m(k_1)$ value based on density value of 1.541 g/cm^3.

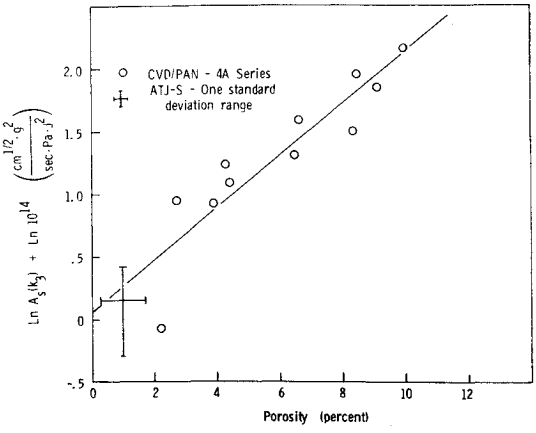

Fig. 7 Relationship between the normalized recession rate $A_s(k_3)$ and porosity for CVD/PAN 4A material.

$A_s(k_1)$ and porosity within the groups is much smaller than between groups and the experimental errors mask the correlations.

The values for $A_s(k_2)$ in Table 2 are essentially constant; variations are within one standard deviation. This observation suggests that those properties that are responsible for attaining thermal and rate equilibration are similar. Similarity in these materials, except for porosity, also is supported by Figs. 4 and 5 where all of the normalized rate constants conform with the log relationships.

A correlation between ablation and porosity for ATJ-S and its precursors is not surprising, since they contain a common filler-binder formulation made from petroleum and coal-tar pitches. The presence of CVD/PAN in this same group shows that the carbon source (in this case, PAN fibers and pyrolytic carbon) is not of major importance. Instead, structural properties such as porosity outweigh formulation considerations.

As noted before, prior to the steady-state phase the highly porous graphites develop very rough surfaces which persist during the steady-state condition. A larger surface area could be responsible, at least in part, for the variation in the values for k_1.

An examination of Eq. (2) and Table 2 shows that this is not correct, since the term $(1-e^{-k_2 t})$, which would be responsible for variations in the initial rates, does not differ in value, within experimental error, for the materials tested. Thus, the initial as well as the steady-state rates are dependent on k_1 which, in turn, is dependent on porosity.

The material in frustum 4A was not as uniform as that in frustum 6A and, therefore, provided the opportunity to examine the effect of a fivefold variation in porosity on ablation performance within a single material. Unfortunately, the ablation data obtained in this test series were not as precise or as extensive in time or recession as those for the 6A series or the other materials. Values for k_1 or k_2 could not, therefore, be evaluated.

A rate constant that could be used for correlation with porosity for the 4A materials was obtained from a plot of the log of the recession vs time. This plot was linear for the first few seconds of ablation, which extended into the steady-state phase, although less precisely than for the cases of k_1 and k_2. The slope, k_3, when normalized for stagnation pressure and bulk gas enthalpy, $A_s(k_3)$, also was exponentially related to porosity for the 4A models (Fig. 7), as well as the other materials. The straight line is a least-squares fit of the 4A data.

No epidiascope porosity data were available for ATJ-S. To compare the 4A data with ATJ-S, mercury porosimetry data were converted to total porosities (open and closed) greater than 4 μm. The mean ablation and porosity data from 14 and 11 models, respectively, and their standard deviation ranges

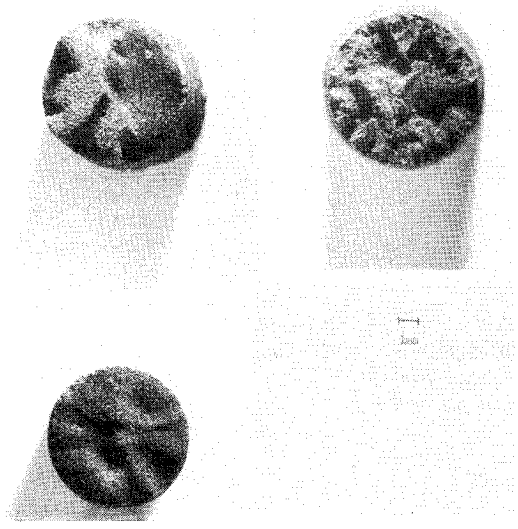

Fig. 8 Representative ablated surfaces. Upper left: ATJ-S precursor, not impregnated; upper right: CVD/PAN; lower left: ATJ-S.

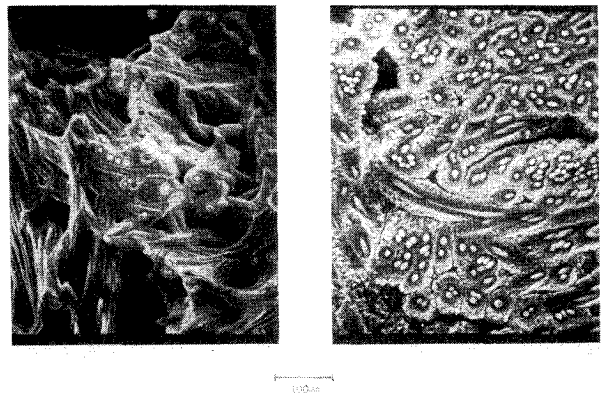

Fig. 9 Scanning electron photomicrographs of a CVD/PAN material. Left: valley on the ablated surface where maximum ablation occurred showing greater porosity, lower fiber density, and smaller interfacial spacing between the fiber and matrix. Right: hill on the ablated surface where minimum ablation occurred showing lower porosity, higher fiber density, and larger spacing between fiber and matrix.

are given in Fig. 7. They show, as in the case of the data in Fig. 3, that ATJ-S and CVD/PAN constitute a single class of ablators with respect to their ablation dependence on porosity. Both figures suggest that a reduction in the CVD/PAN porosity to that in ATJ-S would provide an equivalent ablator.

The ablation performance of CVD graphitic materials was assessed in two additional studies. One involved a CVD/PAN material prepared in plate rather than frustum form. Its density was 1.83 g/cm^3, and it was tested at the McDonnell Douglas HIP facility at a higher stagnation pressure.

The other ablation study was conducted by Sheldahl and Wright[6] in a channel test device at a lower stagnation pressure with CVD/rayon. The ratios of the ablation rates for the CVD materials and ATJ-S are shown in Table 3. The ratio for the CVD/PAN 4A series is based on the lowest $A_s(k_3)$ value (Fig. 7). The variation in the ratios limits the possibility of definitive conclusions concerning the ablation performance of CVD/felt materials relative to ATJ-S, since the graphites and test conditions varied. However, the data imply again that the former have the potential to perform as well as ATJ-S.

Morphology of Ablated Surfaces

A distinguishing feature between the more ablation-resistant materials and those less resistant was the gross

Table 3 Comparative ablation performance of CVD/felt and ATJ-S materials

Test facility	Fiber	$Pa \times 10^{-6}$	$J/g \times 10^{-3}$	Recession rates CVD/felt/ATJ-S
Sandia 2-MW impact	PAN (4A series)	2.3–2.4	5.2–5.4	1.0
Sandia 2-MW impact	PAN (6A series)	2.2–2.5	5.0–5.8	3.2
McDonnell Douglas	PAN	10.3	4.65	1.3
Sandia 2-MW channel test device	Rayon	4.7	20.1	1.0

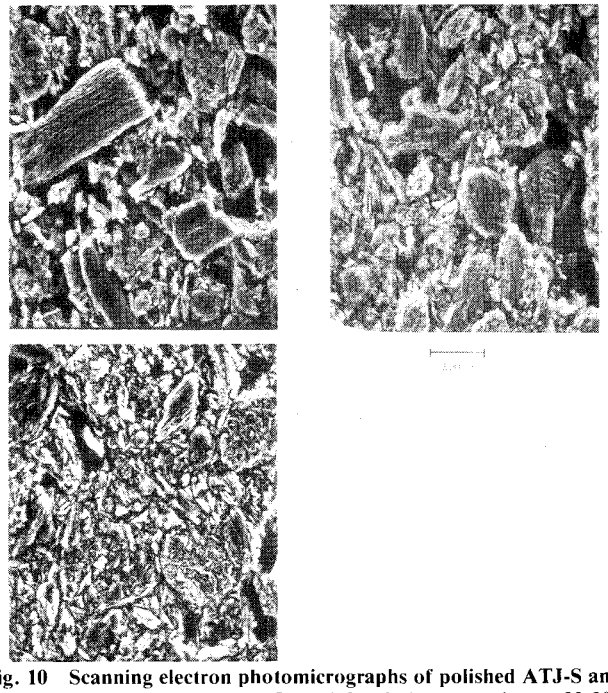

Fig. 10 Scanning electron photomicrographs of polished ATJ-S and precursor graphite surfaces. Top left: 0 impregnations, 33.3% porosity; top right: 1 impregnation, 24.8% porosity; bottom left: 2 impregnations, 20.6% porosity.

roughness of the ablated surface. In the previous section, it was suggested that porosity rather than gross surface roughness was responsible for the variation. It was, therefore, of interest to examine the surfaces microscopically to gain further insight on how structure relates to ablation performance. Both scanning electron microscopy (SEM) and light microscopy were used.

Figure 8 shows representative ablated surfaces of three models in which oblique lighting was used to enhance surface roughness. It is evident that roughness increases with porosity. To determine the causes, hills and valleys where minimum and maximum ablation occurred were examined with SEM. For the CVD/PAN models, three factors were found which correlate with nonuniform ablation: porosity, fiber density, and the fiber-matrix interfacial spacing.

Figure 9 (left) is a photomicrograph of a rare valley in which all three factors occur, i.e., high porosity, low fiber density, and small fiber-matrix interfacial spacing. Figure 9 (right) shows a representative hill where minimum ablation occurred for comparison. For the ATJ-S and its precursor-type graphites, porosity appears to be the predominant factor in influencing ablation rate and nonuniform ablation. Figure 10 shows SEM examples of ablated surfaces from ATJ-S and its precursors.

Conclusions

A comparative study of the ablation performance of CVD/PAN, ATJ-S, and ATJ-S precursor graphites in an arc jet environment provided the following conclusions:

1) Ablation kinetics can be characterized by an initial nonlinear phase, during which thermal and chemical equilibrium are approached, and a subsequent steady-state phase, during which the ablation rate is constant.

2) The kinetics can be modeled with a relationship in which the initial phase is exponential and the subsequent phase is linear.

3) The rate constants for the linear phases of all of the preceding materials are related exponentially to their porosities. The rate constants for the nonlinear phases are constant. The latter result shows that the properties on which thermal and chemical equilibrium are dependent are very similar for the preceding materials.

4) The densities of these materials below the ablated surfaces (~ 5 mm) correspond to their bulk densities, with the exception of CVD/PAN 6. This material apparently decreases in density from an initial value of 1.811 to 1.541 g/cm^3.

5) Gross surface roughness or nonuniform ablation is related to porosity. Although the ablation rate might be expected to be related to gross surface roughness, the measured ablation rate appears to be more highly dependent on porosity.

6) A microscopic investigation of surfaces before and after ablation shows that surface roughness correlates with porosity distribution, fiber density, and the fiber-matrix interfacial spacing.

7) CVD/felt appears to have the potential for improved ablation performance if its porosity can be reduced.

Acknowledgments

This work was supported by the U.S. Energy Research and Development Administration. The authors gratefully acknowledge the contributions of G.T. Noles and J.F. Smatana for the preparation of the CVD/PAN composites, K.L. Goin and G.F. Wright, Jr. for the ablation testing, S.F. Duliere and J.F. Maurin for the scanning electron microscopy, J.B. Duran for the metallography, and A.E. McIntyre for computer programming.

References

[1] Auerbach, I., Lieberman, M.L., Lawson, K.E., and Pierson, H.W., "Effects of Porosity and Structure of Graphite Materials on Ablation in Arc Generated Plasmas," Sandia Laboratories, Albuquerque, N. Mex., SAND 76-0176, July 1976.

[2] Goin, K.L., "Performance and Operation of the High Pressure Arc Heater of the Sandia 2-Megawatt Plasma-Jet Facility," Sandia Laboratories, Albuquerque, N. Mex., SC-DR-72-0521, Dec. 1972.

[3] Williams, R.R., "High Impact Pressure (HIP) Facility Test Stream Calibration Results," McDonnell Douglas Research Laboratories, St. Louis, Mo., MDC-Q-0467, May 1972.

[4] Lieberman, M.L., Curlee, R.M., Braaten, F.H., and Noles, G.T., "CVD/PAN Felt Carbon/Carbon Composites," *Journal of Composite Materials,* Vol. 9, Oct. 1975, pp. 337–346.

[5] Fisher, C.F., "The New Quantimet 720," *Microscope,* Vol. 19. 1971, pp. 1–20.

[6] Sheldahl, R.E. and Wright, G.F., Jr., "MTV Antenna Joint Ablation and Heat-Transfer Rate Study in a Confined Channel," Sandia Laboratories, Albuquerque, N. Mex., SC-DR-70-298, June 1970.